Electronically engineering microstructural design for developing advanced steels An exploration of high Si bainitic steel

Xing, Xiaolei; Li, Yawen; Meng, Shuo; Shi, Zhijun; Zhou, Yefei; Yang, Qingxiang; Xiao, Jianwei; Zhu, Yuntian; Deng, Chuang

Published in:
Materials and Design

Published: 01/09/2022

Document Version:
Final Published version, also known as Publisher's PDF, Publisher's Final version or Version of Record

Published version (DOI):
10.1016/j.matdes.2022.111011

Publication details:
Xing, X., Li, Y., Meng, S., Shi, Z., Zhou, Y., Yang, Q., Xiao, J., Zhu, Y., & Deng, C. (2022). Electronically engineering microstructural design for developing advanced steels: An exploration of high Si bainitic steel. *Materials and Design*, *221*, Article 111011. https://doi.org/10.1016/j.matdes.2022.111011

Materials & Design 221 (2022) 111011

Contents lists available at ScienceDirect

Materials & Design

journal homepage: www.elsevier.com/locate/matdes

Electronically engineering microstructural design for developing advanced steels: An exploration of high Si bainitic steel

Xiaolei Xing [a,1], Yawen Li [b,1], Shuo Meng [a], Zhijun Shi [c], Yefei Zhou [a,c,*], Qingxiang Yang [c], Jianwei Xiao [d,e,*], Yuntian Zhu [d], Chuang Deng [e,*]

[a] College of Mechanical Engineering, Yanshan University, Qinhuangdao 066004, China
[b] State Key Laboratory of Superhard Materials, Key Laboratory of Automobile Materials of MOE, and School of Materials Science, Jilin University, Changchun 130012, China
[c] State Key Laboratory of Metastable Materials Science & Technology, Yanshan University, Qinhuangdao 066004, China
[d] Department of Materials Science and Engineering, City University of Hong Kong, Hong Kong, China
[e] Department of Mechanical Engineering, University of Manitoba, Winnipeg, MB R3T 5V6, Canada

HIGHLIGHTS

- >Si addition in bainitic steel leads to a novel FCC-to-BCC phase transformation due to large lattice distortion and Jahn-Keller splitting.
- >ELF in γ-Fe can be increased by Si addition, which in turn improves its thermal stability and stacking fault energy.
- >Excellent resistance against elastic strain and wear can be achieved in the laser melting bainitic layer with Si addition.
- >Microstructures of engineering materials can be designed by tailoring their electronic structures.

GRAPHICAL ABSTRACT

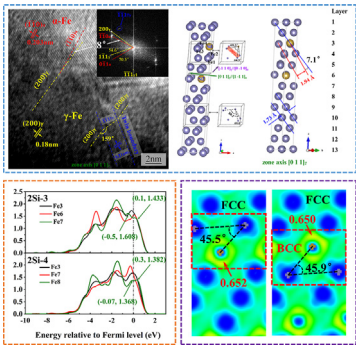

ARTICLE INFO

Article history:
Received 19 April 2022
Revised 13 July 2022
Accepted 30 July 2022
Available online 1 August 2022

Keywords:
Bainitic steel
Electronic structure
HRTEM
Density functional theory (DFT) simulations

ABSTRACT

Microstructure engineering is essential for developing advanced steels and is often carried out by thermomechanical processing. Here we report the engineering of microstructures of a high Si bainitic steel by tuning its electronic structure. It is experimentally found that the bainitic steel with Si addition processed with laser melting has a complex multiphase microstructure consisting of α-Fe, γ-Fe, ε-martensite, and nano-scale twin boundaries with significantly improved hardness. Furthermore, calculations based on density functional theory show that the observed microstructure is strongly correlated with changes in the electronic structures of Fe atoms around the Si impurities. In particular, electron localization around the Si impurities significantly alters the stacking fault energy, which promotes the formation of ε-martensite and nanoscale twin boundaries, while the Jahn-Teller splitting caused by Si dopants results in a FCC-to-BCC phase transition with a misorientation angle of 8° between the $(200)_\gamma$ and $\left(\bar{1}\,1\,0\right)_\alpha$. This work suggests that controlling the microstructures by electronic structure engineering has great potential for designing new structural materials with excellent mechanical properties.

* Corresponding authors at: College of Mechanical Engineering, Yanshan University, Qinhuangdao 066004, China (Y. Zhou). Department of Materials Science and Engineering, City University of Hong Kong, Hong Kong, China (J. Xiao).
E-mail addresses: yfzhou@ysu.edu.cn (Y. Zhou), jianxiao@cityu.edu.hk (J. Xiao), Chuang.Deng@umanitoba.ca (C. Deng).
[1] These authors contributed equally to this work.

https://doi.org/10.1016/j.matdes.2022.111011
0264-1275/

1. Introduction

The correlation between microstructures and mechanical properties governs the design and application of structural materials [1]. Structural materials are mostly polycrystalline whose crystal structures are strongly influenced by the atomic bonding and coordination number [2,3]. Since the atomic bonding is formed by gaining/losing or sharing electrons between neighboring atoms and the coordination number is quantitatively related to the state of the valence electrons, the electronic structures should ultimately decide crystal structures in their atomic or molecular components [4–6]. Previous experimental and theoretical works have reported the direct correlation between crystal structure and electronic states [7,8]. For example, Sun et al. [9] have studied the relationship between electron localization and structural transformation in alkali and alkaline earth metals and found that under high pressure, the site of electron localization changes when the lattice constant decreases, which results in body-centered cubic (BCC)-to-simple cubic (SC), face-centered cubic (FCC)-to-hexagonal close-packed (HCP), and other types of transformations. Besides, by analyzing the valence electron state of the atomic component of medium and high entropy alloys, Chen et al. [10] have successfully predicted their crystal structures and short-range order.

Apart from structure prediction, the mechanical properties of materials can also be understood in the matter of electronic structures [11–13]. For example, the elastic modulus of a material is related to the bonding type, and the electron density in atomic bonds determines the material's strength [14]. Based on this concept, an equation has been constructed to successfully predict the hardness of covalent bonding materials [15]. Furthermore, the different ideal strengths among FCC, BCC, and HCP metals can also be explained in terms of electron localization. With regard to plasticity, the stacking fault energy is a fundamental parameter in determining the plastic deformation mechanism of FCC metals and alloys [16,17]. For example, as the stacking fault energy (SFE) decreases, there is a transition in dominating plastic mechanism from perfect dislocation slip (i.e., SFE > 45 mJ/m^2) to twinning and partial dislocation slip (i.e., SFE = 15–45 mJ/m^2) and finally to martensitic transformation (i.e., SFE < 15 mJ/m^2) [18,19]. The SFE for metals and alloys is directly related to electronic structures because stacking fault formation involves bond breaking and formation [20,21]. Therefore, plasticity is also an electronic related property.

Nevertheless, despite the seemingly strong and clear correlation between the electronic structure of materials and their crystal structure and mechanical properties, the idea of electronic structure engineering has been mainly limited to semiconductors to tailor their electrical and optical properties in the past [22,23]. In this work, we show that it is possible to engineer microstructures of a high Si bainitic steel for better mechanical properties with the help of tuning electronic structures, which demonstrates the potential of electronic structure engineering as a general strategy to guide the design of microstructures in conventional structural materials.

A bainitic steel is studied here since bainite is an important component of many advanced high-strength steels (AHSSs) [24,25]. AHSSs have received a growing interest in recent years due to their great potential to meet the combined requirements of weight reduction and performance improvement [26,27]. Fine grain strengthening and dislocation strengthening are the mainstream approaches to strengthen AHSSs [28,29]. However, these methods usually sacrifice the ductility of steel. For example, the widely used laser melting technology for improving the strength of AHSSs introduces a high density of dislocations and refines the microstructure through instantaneous heating and cooling, but it causes high residual stresses and leads to the formation of hard martensite [30,31]. Therefore, after the laser melting process, a long incubation period of bainitic isothermal transformation (i.e., above the martensite start (*Ms*) temperature) is needed to avoid the martensite transformation so that the steel remains in the state of supercooled austenite, thus reducing the laser melting stress by virtue of the excellent plasticity of austenite [32,33]. Alternatively, twin boundary strengthening has been demonstrated as an effective method to simultaneously improve the strength and ductility of metals [34,35].

It has been previously reported that Si addition can significantly reduce the energy barrier of twin formation in steel (e.g., from 642.0 mJ/m^2 away from the Si dopants to 115.1 mJ/m^2 around the Si dopants) [36]. In addition, previous experiments and theoretical calculations based on density function theory (DFT) have shown that the addition of Si can suppress the formation of the brittle cementite in AHSSs [37]. This work deepens the understanding of microstructural evolution in steel from the physical point of view and provides a practical strategy to control the microstructures of materials by tailoring their electronic structures.

2. Materials and methods

2.1. Experimental methods

A steel ingot with a chemical composition of Fe-0.54C-2.53Si-1.82Mn-1.08Cr-0.45Ni-0.32Mo was prepared by smelting and then homogenized at 1200℃ for 4 h. The ingot was then austenitized at 1000 °C for 15 min and isothermally transformed at 250 °C for 24 h to obtain a bainite microstructure. After that, the steel samples with the dimension of 40 × 20 × 10 mm^3 were machined and cleaned in ethyl alcohol. The machined samples were then laser remelted and followed by isothermal transformation at 250 °C for 24 h. The laser power outpt is 1.8 kW, laser scanning speed is 10 mm/s and laser spot diameter is Φ3.0 mm. Field emission scanning electron microscopy (FESEM, Hitachi S4800) was used to examine the microstructures of the samples. X-ray diffractometer (XRD, D/max-2500/PC) with Cu Kα radiation at 40 kV and 20 mA was performed to determine the phase constitution. During the test, 40° < 2θ < 120° with a step size of 0.02° was set and the collection time was 2 s. TEM and high resolution TEM (HRTEM) (Tecnai G2 F30 S-NANO-TWIN) with the accelerating voltage of 200 kV were used to analyze the microstructure of the laser-melted surface layers. The thin sheet with a thickness of nearly 400 μm was cut from the laser-melted surface layer, which was then ground to a thickness of 20 ~ 30 μm with sandpapers. Finally, the ion milling (Gatan 691) was used to obtain an electron transparent thin area. The hardness was measured by nano-indentation tests using an NHT^2 apparatus from Anton Paar instruments equipped with a Berkovich indenter. The results were determined using the load of 10 mN and the dwell time of 10 s. The indenter has been calibrated by indenting fused silica between each sample. The nano-hardness was measured based on 225 indentations (a regular array of 15 × 15 indentations covering a 70 × 70 μm^2 area) for surface layers both with and without laser melting. Sliding wear tests of the samples were carried out using a reciprocating friction tribometer (Anton paar tribometer) under unlubricated dry conditions to ascertain changes in the tribological behavior. The sliding wear test sample size was 12 × 6 × 3 mm^3. The load, liner speed, test distance, and times of the wear test were 5 N, 40 mm/s, 8 mm, and 60 min, and a 6 mm diameter tungsten carbide ball was used for sliding against the sample.

2.2. DFT calculations

The total energy of each model was calculated by the Cambridge Sequential Total Energy Package code (CASTEP) based on

DFT [38]. The exchange–correlation functional was the Pardew–Burke–Ernzerh (PBE) [39] version of the generalized gradient approximation (GGA). The plane-wave cutoff energy was set as 600 eV. The convergence parameters were set as follows: the total energy tolerance was 5×10^{-6} eV/atom, the force tolerance was 0.01 eV/Å, the maximum stress component was 0.02 GPa, and the maximum displacement was 0.0005 Å. After enough volumetric relaxation and energy convergence test, a $6 \times 10 \times 1$ k-point sampling mesh was used for each supercell together with a smearing width of 0.2 eV for the Methfessel-Paxton scheme. The optimized structures by CASTEP were continuously optimized by using VASP [40,41] with the same setup as in CASTEP to calculate the electron localization function (ELF). The optimized structures by using VASP were the same as those optimized by CASTEP.

The supercell was created from the FCC unit cell in $\left[11\bar{2}\right]_\gamma$, $\left[\bar{1}10\right]_\gamma$ and $[111]_\gamma$ directions. The supercell of the Fe and Fe-Si systems consists of 12 layers and ABCABCABCABC stacking sequence of close-packed planes. In this paper, the C atom was incorporated as an interstitial impurity in an octahedral site of the FCC Fe-Si supercell. The relaxation was terminated when the convergence criteria were met.

The generalized stacking fault energy (GSFE) with the fault vector u_z ($\gamma_{GSF}^{u_z}$) was calculated by.

$$\gamma_{GSF}^{u_z} = \frac{E(u) - E_0}{A} \quad (1)$$

where $E(u)$ is the total energy of the supercell with the fault vector u_z, E_0 is the total energy of the perfect FCC supercell and A is the area of the fault plane.

3. Results

3.1. Microstructural analysis

The microstructures of the samples with Si element but without laser melting consist of mainly bainite ferrite and residual austenite with film and blocky morphology and the overall phase ratio is roughly 80:20 between ferrite and austenite (Supplementary Figs. S1 (a), S1 (c) and S2). Through instantaneous heating and cooling by laser melting, a melting layer with an average thickness of 232 μm was prepared, and the ultra-fine structure was obtained by eliminating the submicron blocks of residual austenite in the laser melting layer (Supplementary Figs. S1 (b)). The nano-twin in the residual austenite and ε-martensite with HCP structure were detected only in the laser melting layer which was supported by XRD and TEM analysis (Supplementary Figs. S1 (d) and S2). Meanwhile, the thermal stress during the laser melting served as a driving force to form the nano-twin and the ε-martensite in this medium-carbon high-silicon steel. These results indicate that Si element along with subsequent laser melting induced the formation of multiphases in this steel with γ-Fe, α-Fe, ε-martensite, and nanoscale twins. The nano-twin structures and ε-martensite can be obtained on the premise that the formation of cementite is replaced by carbon-rich residual austenite during bainite transformation.

The microstructure of conventional bainitic steel (e.g., without Si element) mainly consists of ferrite (α-Fe, BCC) and cementite (Fe_3C) [42]. A dramatically different microstructure of the laser-melted sample with Si doping was observed in this work by using TEM, as shown in Fig. 1. As indicated in Fig. 1(a), strong diffraction spots emerged with respect to the $(111)_\gamma$ plane of the FCC structure along with diffuse spots in the $[110]_\gamma$ direction, which suggests the formation of twins in γ-Fe. In addition, α-Fe was found to be in contact with the retained austenite with a 4.5° orientation difference between $\left(11\bar{1}\right)_\gamma$ and $\left(\bar{1}0\bar{1}\right)_\alpha$. Additionally, ε-martensite (HCP) was formed as shown in Fig. 1(b) with the lattice parameters determined to be a = 2.5 Å and c = 3.9 Å by the corresponding diffraction pattern. No cementite was found, which is consistent with previous reports that Si dopants can suppress the formation of cementite in AHSSs.

An HRTEM image of the intersection region of the retained austenite and the nano twins is shown in Fig. 2. The HRTEM image and Fourier transformation image reveal that this region consists of both FCC and BCC structures but the BCC structure only exists in the upper section. The nano-twin detected at the lower section shows an ultrafine structure with a thickness of only ~ 2 nm. Moreover, the corresponding diffraction pattern of the intersection region in Fig. 2(a) shows that the diffraction spots of $\left(11\bar{1}\right)_\gamma$ and $\left(\bar{1}0\bar{1}\right)_\alpha$ crystal planes and $\left(1\bar{1}1\right)_\gamma$ and $\left(0\bar{1}1\right)_\alpha$ crystal planes do not coincide. The results suggest that the orientation between the γ- and α-Fe did not fully comply with the traditional Kurdjumov–Sachs (K–S) relationship [43] (i.e., $\left\{11\bar{1}\right\}_\gamma \| \{011\}_\alpha$ or $<\bar{1}01>_\gamma \| <\bar{1}\,\bar{1}\,1>_\alpha$) in bainitic steels. The interplanar spacing and intersection angle were furtherly measured to analyze the relationship between the FCC and BCC phases, as marked in Fig. 2(b). The interplanar spacing of $(200)_\gamma$ and $\left(\bar{1}\,\bar{1}0\right)_\alpha$ are 0.18 nm and 0.203 nm, respectively, which are consistent with the corresponding diffraction pattern in Fig. 2(a). The angle between the $(200)_\gamma$ in γ-Fe and $\left(\bar{1}\,\bar{1}0\right)_\alpha$ in α-Fe is 8°.

3.2. Mechanical property

The hardness and its distribution in the laser melting layers compared to those without laser melting are showen in Table 1 and Fig. 3. The laser melting layers in steel show a significantly higher hardness (~7.8 GPa) than their counterparts without laser melting (~6.6 GPa). It needs to be mentioned that the hardness of bainite ferrite is usually higher than that of the residual austenite, and the elastic modulus of retained austenite is lower than that of BCC (or even body-centered tetragonal (BCT) [44]) bainite ferrite due to its FCC crystal structure. Therefore, the residue austenite is mainly used to improve the toughness of bainite steels because of its good plasticity. Since laser melting can increase the strength by refining the microstructures and introducing a high density of dislocations, as mentioned earlier, it is important to justify how the increased hardness in the laser melting layer may be related to the formation of nano-twin and ε-martensite structures as revealed by TEM analysis (Figs. 1 and 2). As shown in Table 1, the hardness and elastic modulus of the main matrix is averaged after removing the nano-indentation results of the hard points (in the sample with laser melting) or the soft points (in the sample without laser melting). Compared with the sample without laser melting, the elastic modulus of the main-matrix in the laser-melted sample decreases from 223 to 221 GPa while its hardness increases from 7.02 to 7.69 GPa, which suggests that while laser melting induced microstructural refinement can indeed influence the hardness and elastic modulus, the effects are not strong enough to explain the observed high hardness (e.g., 9.46 GPa) in the laser melted sample. Furthermore, the high hardness in the laser melting layer exhibit an overall low elastic modulus while for samples without laser melting, the points with higher hardness also have higher modulus. For example, the sample without laser melting has a higher elastic modulus in the matrix (~223 GPa) than that in the low hardness points (~215 GPa), suggesting that the low hardness is mainly associated with FCC structure while the matrix

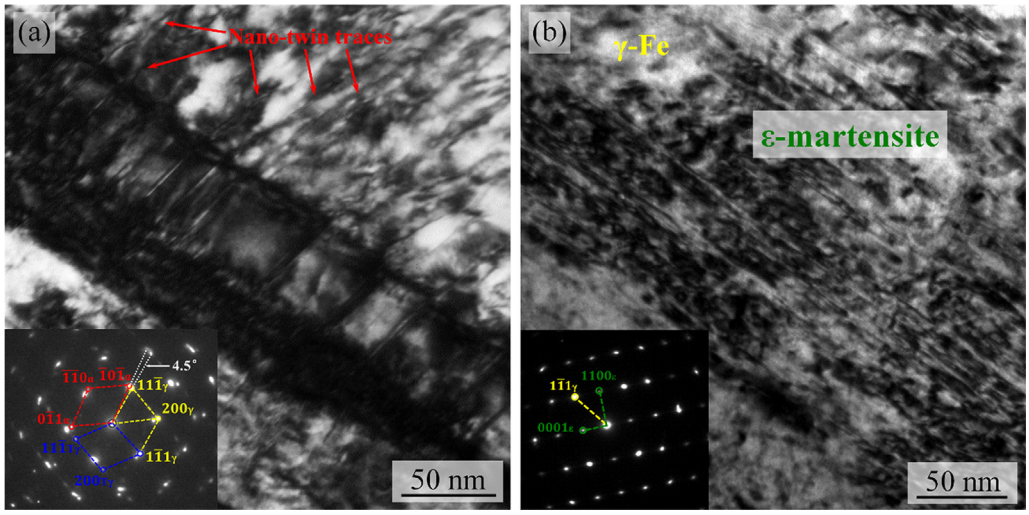

Fig. 1. Microstructural analysis by TEM showing (a) nanoscale twins in γ-Fe (FCC) and nano-twin traces in α-Fe (BCC) and (b) ε-martensite (HCP).

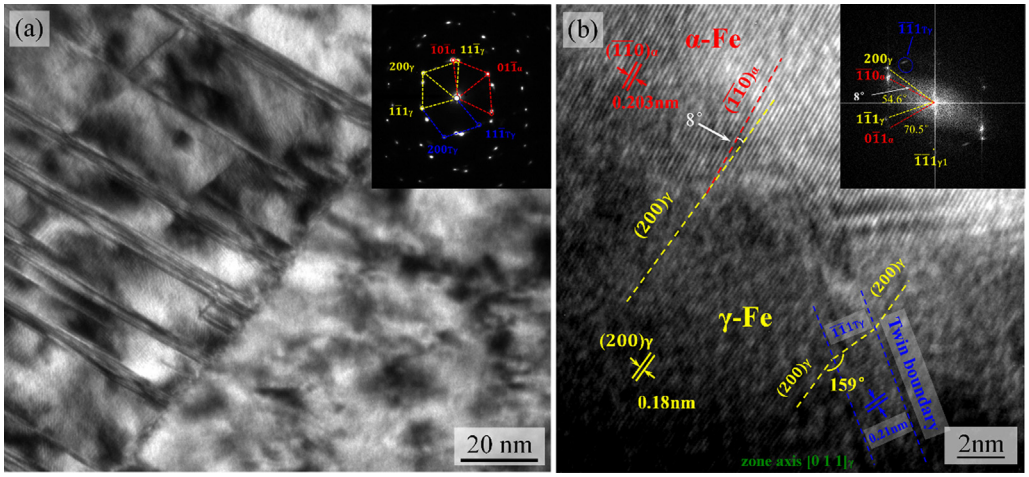

Fig. 2. (a) TEM and (b) HRTEM analysis of the structure at the phase interface between nanoscale twins in γ-Fe and α-Fe.

Table 1
Indentation hardness and elastic modulus of with and without laser melting layer.

Samples	Main matrix		High hardness points		Low hardness points	
	Hardness (GPa)	Elastic modulus (GPa)	Hardness (GPa)	Elastic modulus (GPa)	Hardness (GPa)	Elastic modulus (GPa)
With laser melting	7.69 ± 0.36	220.83 ± 9.94	9.46 ± 0.41	217.55 ± 9.4386		
Without laser melting	7.02 ± 0.17	223.22 ± 5.35			6.35 ± 0.24	215.35 ± 7.36

is mainly BCC. In contrast, the elastic modulus of high hardness points in the laser melting layers (~217 GPa) is lower than that of the main matrix (~220 GPa). It is also noted that the elastic modulus of the high hardness in the laser-melted sample (~217 GPa) is close to that for the low hardness in the sample without laser melting (~215 GPa). It can thus be inferred that the improvement of hardness in the laser-melted layers is mainly related to the formation of nano-twin and ε-martensite structures in the retained austenite with FCC structure.

Previous studies have shown that both high hardness (H) and low elastic modulus (E) can improve the resistance of the surface layer to mechanical degradation and failure [45]. In this regard, a high H/E ratio (resistance against elastic strain to failure) is advisable, as it means that the material is "elastic strain to failure" for a longer time to allow the applied load to be redistributed over a large area, delaying the failure of the surface layer. A high H^3/E^2 ratio (resistance against plastic deformation) is also essential because it indicates the crack resistance of the coating. Compared to the sample without laser melting, the H/E values of the sample with laser melting increased from 0.0308 to 0.0358. The H^3/E^2 ratios follow a similar evolutionary trend to that of the H/E ratios, and the H^3/E^2 ratios are 0.0064 and 0.010 for the sample without and with laser melting , respectively.

Compared to those without laser melting, the wear volume loss and scar outlines of the wear track in the laser melting layers are plotted in Supplementary Fig. S3. As can be seen from the scar outlines of the wear track after the wear test, the laser melting layers in steel show a significantly higher wear resistance than their counterparts without laser melting. Compared with the sample without laser melting, the wear volume loss of the laser-melted

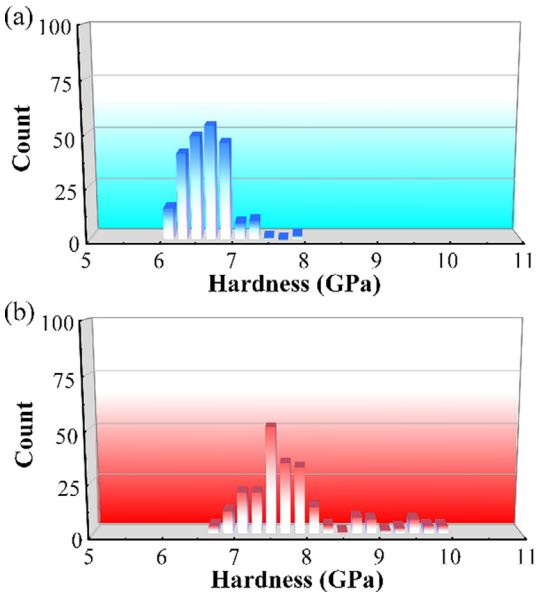

Fig. 3. Hardness distribution in the high Si bainitic steel surface layer: (a) without laser melting; (b) with laser melting.

sample decreases from 1.142 mm^3 to 0.675 mm^3. The wear volume reduction ratio of the sample with laser melting is 40.9 %.

3.3. Si-induced microstructure evolution based on DFT calculation

Based on the above results, the microstructural evolution in bainite steel is mainly induced by Si dopants. Therefore, to study the unconventional FCC-to-BCC phase transformation mechanism, the influences of Si on the crystal structures of γ-Fe were studied using DFT. According to the symmetry of the structure, a single Si atom was first added to replace a Fe atom randomly. A second Si or C atom was then introduced into different atomic layers in the supercell and geometrically optimized.

To distinguish the different structures, the structures studied in this paper are referred to as *a*Si-*b*-*cd* according to the number of Si atoms and separation distance between them, where *a*, *b*, *c*, and *d* are values representing the number of Si atoms in the supercell, the distance between $(111)_\gamma$ crystal planes of two Si atoms in the supercell, the distance between the C and the first Si atom, and the position of C atom doping into the octahedral gap, which will be described later.

Fig. 4 shows the morphology of structure 2Si-3 after geometric optimization by DFT calculations. As can be seen from Fig. 4(a), there is a significant change in the local atomic structure after geometric optimization and the lattice distortion mainly occurs around the Si atoms. The interatomic distance between the Si1 atom and Fe1/Fe3 is 2.323 Å/2.398 Å, which is significantly smaller than the interatomic distance (2.432 Å) in pure Fe with an austenite structure. The angles of Fe1-Si1-Fe3 and Fe1-Si1-Fe2 are 69.3° and 64.5°, respectively, which are also different from those in pure Fe with austenite structure (88.1° and 60.0°). To better visualize the lattice distortion, we rotated the supercell to make the observed plane perpendicular to $\left[\bar{1}\,11\right]_\gamma$, as shown in Fig. 4(b). The angle between the $(111)_\gamma$ and $(002)_\gamma$ crystal planes away from Si dopants was measured to be 53.3° after geometric optimization, as shown in Fig. 4(b), which is close to that shown in Fig. 1 (54.7°) based on selected area electron diffraction. Due to local distortion, the angle between the two faces became approximately perpendicular (84.6°) around Si1. It can be concluded that $(111)_\gamma$ and $(002)_\gamma$ are more inclined to transform into $\left(\bar{1}\,01\right)_\alpha$ and $(101)_\alpha$ due to Si-induced lattice distortion, which results in a local FCC-to-BCC transformation.

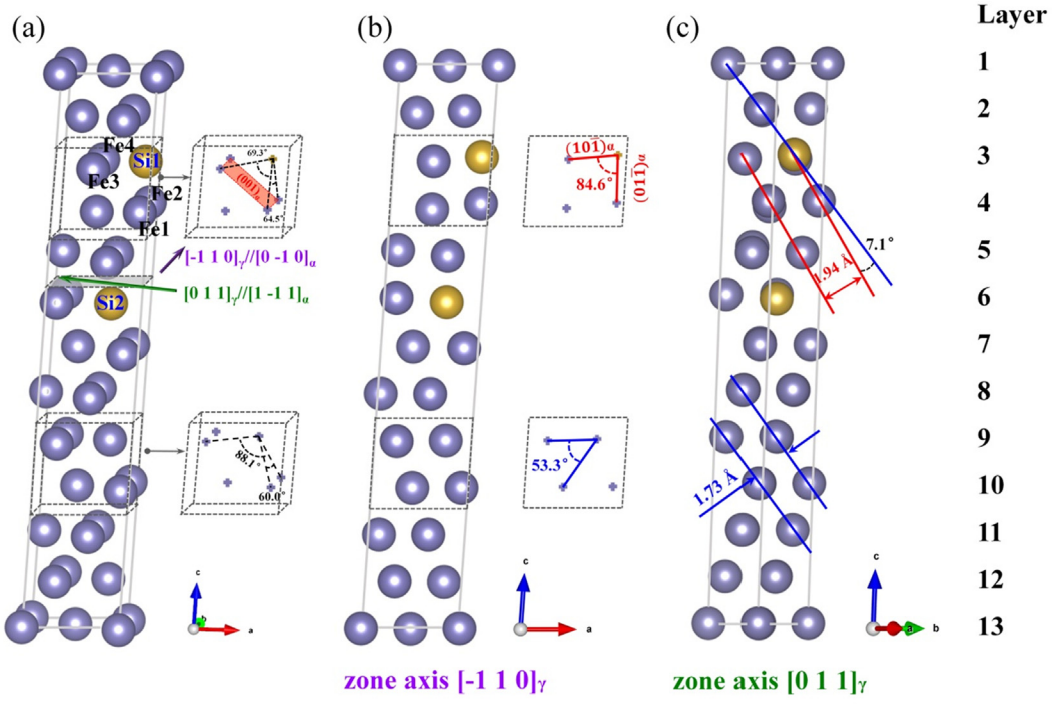

Fig. 4. Morphology of the supercell 2Si-3 after geometric optimization by DFT calculations. (a) The three dimensional structure; (b) the two-dimensional projection along $\left[1\,11\right]_\gamma$ direction; (c) the two dimensional projection along $[011]_\gamma$ direction. The grey and yellow atoms represent Fe and Si, respectively.

In Fig. 4(c), the supercell was rotated to make the observed plane perpendicular to$[011]_\gamma$, which is the same as the zone axis of HRTEM shown in Fig. 2(b). The interplanar spacing of $\left(\bar{1}\,0\,1\right)_\gamma$ and $\left(\bar{1}\,\bar{1}\,0\right)_\alpha$ are measured to be 1.73 and 1.94 Å respectively based on DFT calculations, which are consistent with TEM results of 1.8 and 2.03 Å. The corresponding angle between $(200)_\gamma$ and $\left(\bar{1}\,\bar{1}\,0\right)_\alpha$ crystal planes is 7.1°, which is also close to the HRTEM results of 8°. Through the above analysis, we found that the first-principles calculations are in excellent agreement with the HRTEM results. Therefore, the misorientation between $(200)_\gamma$ and $\left(\bar{1}\,\bar{1}\,0\right)_\alpha$ crystal planes was a direct consequence of Si doping other than experimental error. By modifying the Si doping concentration as shown in Supplementary Fig. S4, it is further confirmed that the FCC-to-BCC phase transition can only be formed when the Si atoms are arranged in a special cluster form considering the periodic boundary conditions. This is consistent with the expectation that a large local distortion is needed to induce such phase transformation and make an angle between the $(200)_\gamma$ in γ-Fe and $\left(\bar{1}\,\bar{1}\,0\right)_\alpha$ in α-Fe.

3.4. Lattice distortion induced by Si dopants

To further study the novel FCC-to-BCC transformation, the lattice distortion induced by Si dopants is quantified in terms of atomic displacement. Fig. 5 shows the positions of atoms in the supercell before and after Si doping, in which the black dotted circles represent the position of atoms before the incorporation of Si atoms, and the displacement values of each atom after Si doping along the $\left[11\bar{2}\right]_\gamma$, $\left[\bar{1}\,10\right]_\gamma$ and $[111]_\gamma$ crystal direction are summarized in Supplementary Table S1, respectively. According to Fig. 5, the FCC-to-BCC phase transformation can only be found in 2Si-3 and 2Si-4 where significant lattice distortion (in terms of total atomic displacement) can occur. The total atomic displacement is too small for all other cases to induce a phase transition. It is worth mentioning that the supercell of 2Si-2 with two Si atoms doped within two atomic layer distances shows almost the same magnitude of lattice distortion as that induced by a single Si dopant. This is because the supercell of 2Si-2 is highly symmetric with the Fe6 atom being the symmetric center of the lattice distortion, i.e., the Si1 and Si2 atoms make the Fe6 atom layer move along positive and negative X-direction, respectively.

4. Discussion

4.1. Si addition promotes twin formation and martensite transformation in steel

To understand why Si dopants promote twinning and ε-martensite transformation in the retained austenite, the pathways for twinning and ε-martensite transformation in γ-Fe-Si are studied and compared to γ-Fe and γ-Fe-C structures. For γ-Fe-Si structures, there are two pathways for twinning. Take the 2Si-2 structure as an example, the twin path 1 and 2 are shown in Fig. 6(a) and (b), respectively. For twin path 1, the first slip occurs between the atomic layer 3 (i.e., pure Fe) and 4 (i.e., Fe-Si) along [1 1 2] direction with a displacement of a/6[1 1 2], after which a stacking fault is formed. Then, a twin is formed when the atoms above atomic layer 4 further slip along the 1/6[1 1 2] direction. For twin path 2, a micro twin forms when the atoms above layers 2 and 3 slip along the [1 1 2] direction consecutively. In contrast, when the atoms above atomic layers 1 and 3 slip along the [1 1 2] direction consecutively, the ε-martensite transformation occurs, as shown in Fig. 6(c). For comparison purposes, the twin formation pathways in γ–Fe-C and γ–Fe structures are also studied by following the same procedure as shown in Fig. 6(d) and (e).

The energy pathways for twin nucleation and ε-martensite transformation are plotted in Fig. 7(a). The maximum in the energy

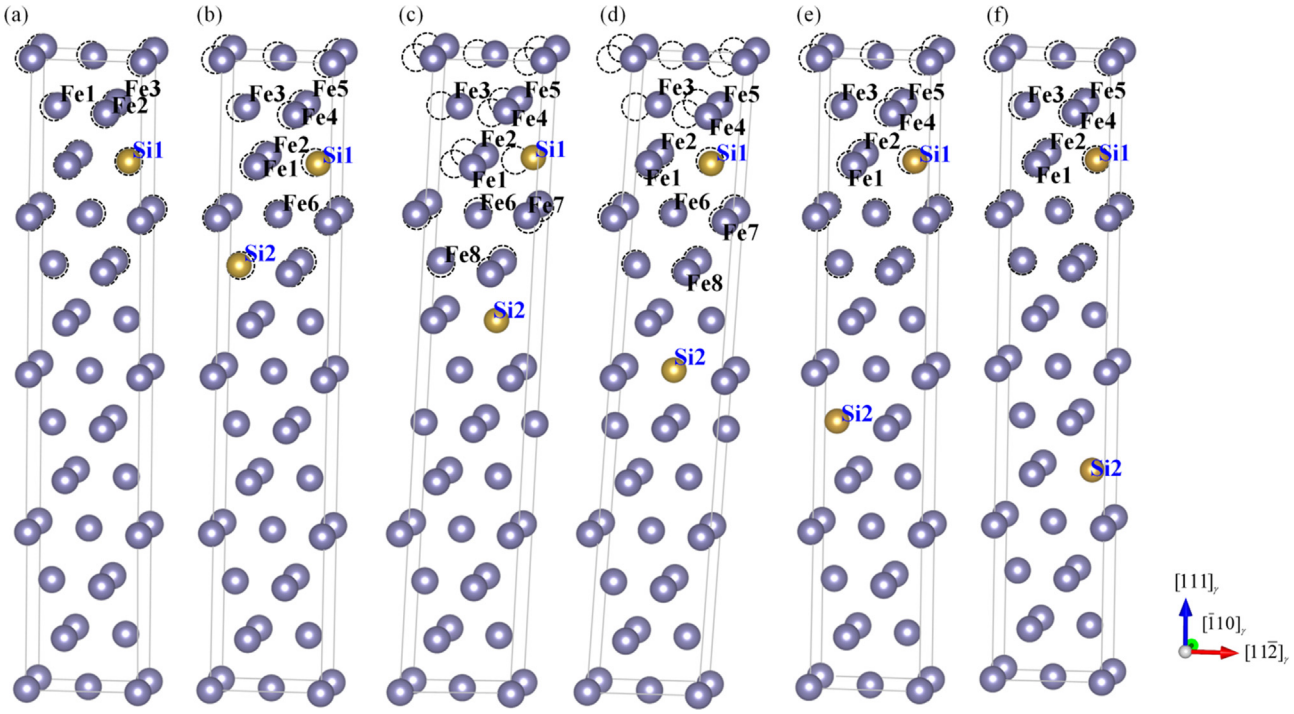

Fig. 5. Schematic diagram of the atom positions in the supercell before and after Si doping: (a) 1Si; (b) 2Si-2; (c) 2Si-3; (d) 2Si-4; (e) 2Si-5; (f) 2Si-6. The dashed circles represent atomic positions before Si doping.

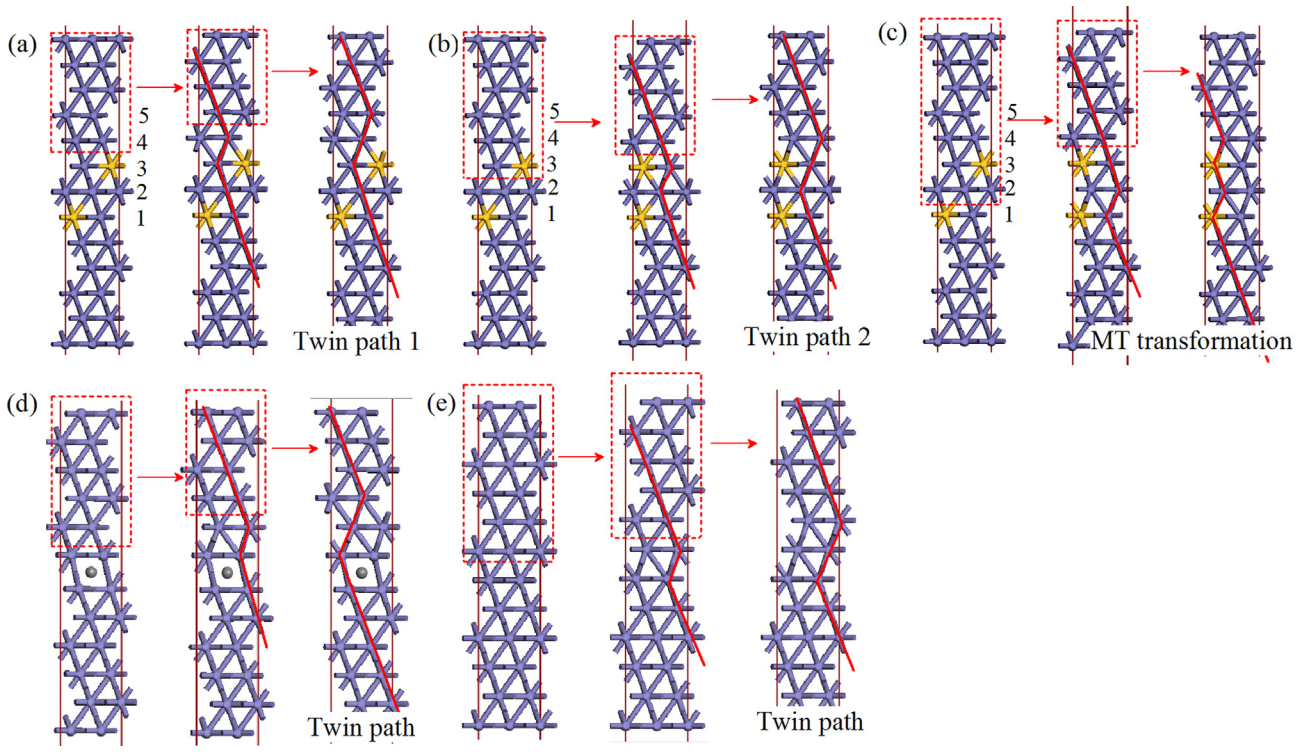

Fig. 6. Pathways for twin and martensitic phase transformation. (a) Schematic for twin pathway 1 in γ-Fe-Si structures. (b) Schematic for twin pathway 2 in γ-Fe-Si structures. (c) Martensite transformation process in Fe-Si structures. (d) Schematic for twin pathway in γ-Fe-C. (d) Schematic for twin pathway in γ-Fe-C.

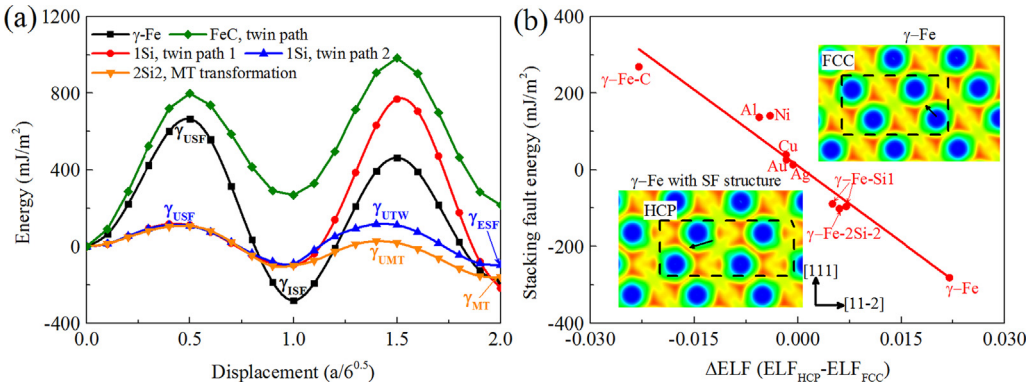

Fig. 7. Twin and martensitic formation in steel. (a) Energy pathways for twin nucleation and martensite transformation in steel. (b) Stacking fault energy as functional of ΔELF between the ELF at the bcp in HCP and FCC structures. The insets in (b) are the electron localization function (ELF) for γ–Fe with and without a stacking fault structure. The blue and red colors represent the minimum and maximum values of ELF in the corresponding FCC structures.

pathway is regarded as the energy barrier for twin or ε-martensite transformations, which is determined to be 744 mJ/m^2 for γ–Fe, 800 mJ/m^2 for γ–Fe-C, and 863 and 205 mJ/m^2 for twin path 1 and 2 for γ–Fe-Si, receptively. It is worth noting that although the γ_{USF} in twin path 1 for γ–Fe-Si (116 mJ/m^2) is much lower than that in γ–Fe and γ–Fe-C structures, their overall energy barriers for twinning are similar since they all involve the slip between atomic planes of pure Fe. In contrast, the stacking fault and micro twin formation in twin path 2 of γ–Fe-Si are both via the relative slipping between the atomic planes of pure Fe and Fe-Si, which significantly reduces the energy barrier as compared to that between atomic planes of pure Fe. For ε-martensitic transformation, it can be regarded as two consecutive stacking fault formation processes. Therefore, the energy barrier γ_{UMT} for ε-martensite transformation in γ–Fe, γ–Fe-C and γ–Fe-Si structures is 665, 798, and 120 mJ/m^2, respectively. By analyzing the interplanar distance between the slip planes, we found that the C dopant decreases the interplanar distance from 2.016 to 1.954 Å. In comparison, the Si atom increases the interplanar distance from 2.016 to 2.039 Å. Therefore, the significantly lower energy barrier for ε-martensite transformation and twin nucleation in γ–Fe-Si structures are both attributed to Si addition by increasing the interplanar distance since it eases the slip between atomic layers as compared to that between pure Fe layers.

It is known that the SFE in a metal or alloy is quantitatively correlated with the difference in the degree of electron localization between the FCC structure and its HCP counterpart [46,47]. Therefore, to explore the physical origin of the SFE in γ-Fe, γ-Fe-Si and γ-Fe-C structures as summarized in Table 2, the electron localization function (ELF) [48–50] at the midpoint of Fe-Fe bond in each structure is studied, which are also summarized in Table 2. In general, the ELF proposed by Becke and Edgecombe can be used to monitor

Table 2
Summary of the ELF at the critical point of Fe-Fe bond in the HCP stacking fault and FCC structures of γ-Fe, Fe-Si, and Fe-C.

	γ_{ISF} (mJ/m^2)	ELF_{HCP}	ELF_{FCC}	ΔELF
γ-Fe	−281.47	0.363	0.341	0.022
γ-Fe-1Si	−95.75	0.367	0.360	0.007
γ-Fe-1Si	−89.08	0.367	0.362	0.005
γ-Fe-2Si-2	−101.53	0.366	0.360	0.006
γ-Fe-C	268.62	0.335	0.358	−0.023

the changes in electron distribution in the bond-forming–bond-breaking processes. For γ-Fe, the SFE (γ_{ISF}) is −281.47 mJ/m^2, and the ELFs at the midpoint of the Fe-Fe bond are 0.363 (ELF_{HCP}) and 0.341 (ELF_{FCC}), respectively, which results in ΔELF of 0.022 between the HCP and FCC structures. Therefore, the stronger ELF between the bonding atoms in the stacking fault structure (HCP) results in the negative SFE in γ-Fe. Furthermore, the negative SFE suggests that γ-Fe is a metastable structure, although the high energy barrier (γ_{USF}) makes the transformation to HCP structure difficult. The ΔELF between HCP and FCC structures in γ-Fe decreases with Si doping, which improves the thermodynamic stability of the FCC structure relative to its HCP counterpart by increasing the SFE from −281.47 to ∼ -90 mJ/m^2. In contrast, by C doping in γ-Fe, the ΔELF between HCP structure and FCC structure changes to −0.023, results in a large positive SFE of 268.62 mJ/m^2.

Based on the the ELF, the SFE of Cu, Al, Ni, Ag, Au, γ-Fe, γ-Fe-C and γ-Fe-Si as a function of ΔELF is plotted as shown in Fig. 7(b).

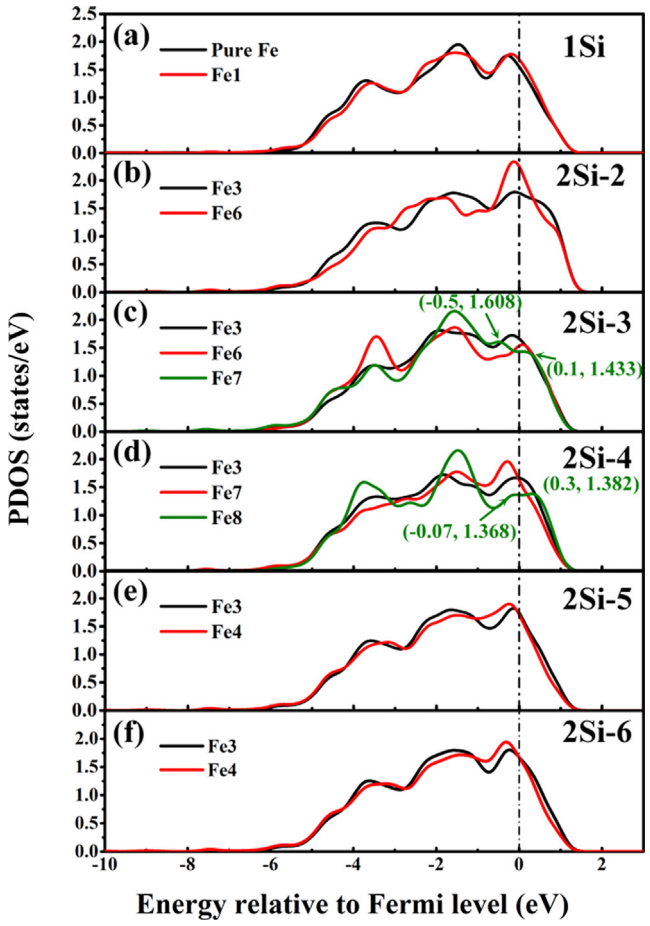

Fig. 8. Electronic density of states of the Fe atoms in six supercells. (a) 1Si. (b) 2Si-2. (c) 3Si-3. (d) 2Si-4. (e) 2Si-5. (f) 2Si-6.

The SFE increases monotonically as the ΔELF increases. It is also shown that when the ΔELF is below (or above) 0, the SFE is positive (or negative). With a simple linear fitting, the relationship between SFE and ΔELF can be expressed as:

$$\gamma_{isf} = -13242\chi \quad (2)$$

where the χ is the ΔELF. This equation builds a simple relationship between the macrophysical properties of a material and its microelectronic structures, which can guide the design of new materials with tunable plastic deformation mechanisms when it is used together with the recently proposed stacking fault energy engineering, e.g., in high entropy alloys.

4.2. The underlying physics of Si doping induced FCC-to-BCC transformation

To explain why large lattice distortion occurred and induced the FCC-to-BCC transformation in the crystal structure around the Si atoms of supercells 2Si-3 and 2Si-4, the electronic density of states (DOS) of the Fe atoms in six supercells was studied with the results shown in Fig. 8. The Jahn-Teller splitting [51,52] effect is well-accepted to be associated with the generation of lattice distortion. The Jahn-Teller theorem indicates that any complex occupying an energy level with electronic degeneracy is unstable, and the asymmetric occupation of electrons in degenerated orbitals leads to the distortion of crystal geometry (A new position of equilibrium is reached in which the local symmetry is lower than the point symmetry of the crystal.) which makes the degenerated energy state split. Therefore, the magnitude of Jahn-Teller splitting will be used as the main criteria to quantify the influences of Si dopants on the lattice distortion of γ-Fe. The black curve in Fig. 8 (a) is the DOS of a Fe atom in the γ-Fe supercell, which shows three peaks in the *d* states below the Fermi level. One of the peaks is slightly lower than

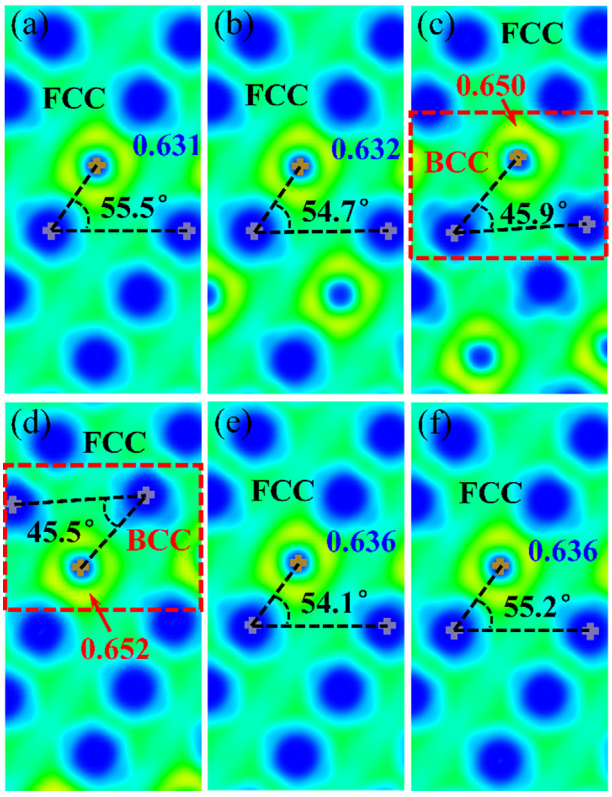

Fig. 9. Electron localization function (ELF) for different supercells. (a) 1Si; (b) 2Si-2; (c) 2Si-3; (d) 2Si-4; (e) 2Si-5; (f) 2Si-6.

the Fermi energy, but no Jahn-Teller splitting was observed. When a Si atom was doped to the supercell (1Si1), the *d* states of the Fe1 atom degenerated more significantly at the Fermi level (red curve in Fig. 8(a)) but showed no Jahn-Teller splitting. Furthermore, with two Si atoms presented in the 2Si-2 supercell, the Fe3 atom has the maximum lattice distortion as shown in Table S1. The large lattice distortion leads to an unprecedented degeneration of the *d* states of Fe3 atom at the Fermi level, as shown in Fig. 8(b). However, there is no Jahn-Teller splitting effect either.

Fig. 8(c) shows the *d* states of the Fe3, Fe6 and Fe7 atoms in supercell 2Si-3. It can be seen that two peaks exist at − 0.5 eV and 0.1 eV in the *d* states of the Fe6 and Fe7 atoms, which indicates Jahn-Teller splitting. For the 2Si-4 structure, as shown in Fig. 8(d), two peaks exist at ∼ − 0.07 eV and 0.3 eV in the *d* states of the Fe8 atom, which also shows *d* state Jahn-Teller splitting. In Fig. 8(e) and (f), the *d* states of the Fe atoms in the supercell 2Si-5 and 2Si-6 show similar DOS to that in the Si1 supercell, i.e., with degeneration at the Fermi level and no Jahn-Teller splitting effect. Therefore, the *d* state Jahn-Teller splitting of Fe atoms in 2Si-3 and 2Si-4 structures and the unconventional FCC-to-BCC phase transformation that we observed from both experiments and DFT calculations are directly correlated. Specifically, through Si doping in a certain configuration, the *d* state Jahn-Teller splitting occurs in such a way that the electrons redistribute around the Fe atoms to remove the degeneracy at the Fermi level caused by large lattice distortion and transform the lattice to a more stabilized BCC structure. These results thus strongly support our proposal that the electronic structure governs a material's crystal structure.

To further confirm the electron redistribution in Fe-Si structures, the ELFs for the six supercells were plotted based on DFT calculations as shown in Fig. 9. A strong merge of ELF around the Si atom was found in all six supercells. This merge reflects the extension of electron clouds around the Si atoms, which improves the stability of the supercell. The ELFs at the middle point of the Fe-Si bond in the transformed BCC lattice of 2Si-3 and 2Si-4 are 0.65 and 0.652, respectively, which are significantly higher than those of FCC structure in the other four supercells (0.631 (1Si), 0.632 (2Si-2), 0.636 (2Si-5) and 0.636 (2Si-6)). Therefore, the FCC-to-BCC transformation can be associated with the higher ELF, and accordingly, stronger electron redistribution, at the critical point of Fe-Si bond in the BCC lattice of 2Si-3 and 2Si-4 than in the FCC counterpart.

4.3. Influence of C atom on FCC-to-BCC phase transformation

To investigate the effect of the low atomic concentration of C compared to Si atom on FCC-to-BCC phase transformation, the C atom was introduced into the Fe-Si structure. According to the

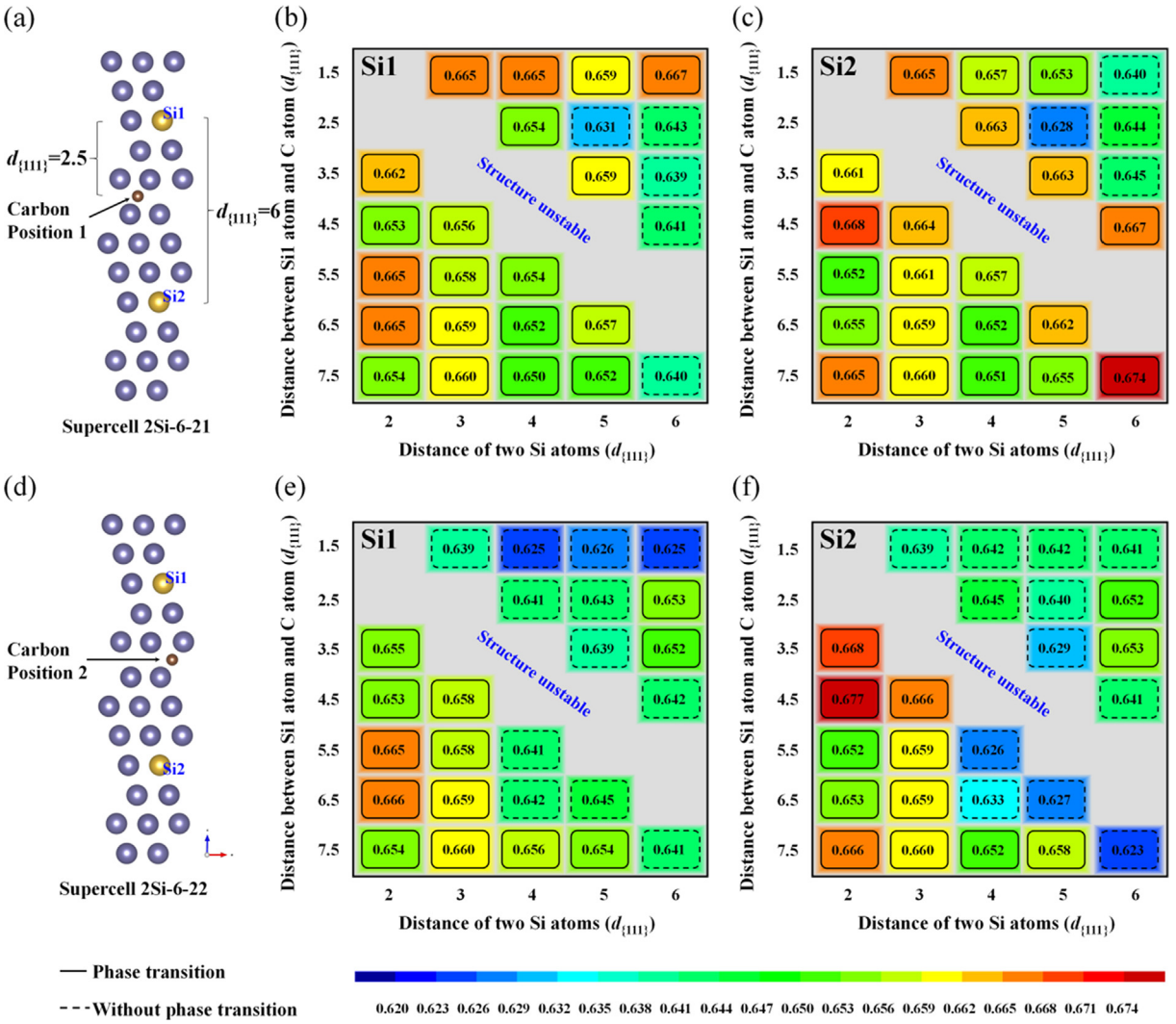

Fig. 10. Summarized FCC-to-BCC structure phase transformation in Fe-Si-C structures. (a) Schematic for C doping in position 1 in 2Si-6. (b) and (c) the ELF with structure phase of Si1 and Si2 location in different structures. (d) Schematic for C doping in position 2 in 2Si-6. (e) and (f) the ELF with structure phase of Si1 and Si2 location in different structures.

mass ratio of C in the modified layer, the number of C atoms in the supercell selected in this paper is calculated to be approximately 1. A single Si atom and carbon atom were added to the supercell and then geometrically optimized. The supercell structure and energy value with the increasing distance between C and Si atoms (Z direction) were plotted, as shown in Supplementary Fig. S5. It is found that the C and Si atoms generally repel each other and the supercell energy reaches a minimum when the distance between Si and C increases to 1.5 $d_{(1\,1\,1)}$. The supercell structure does not change with a further increase in the distance between Si and C and the supercell energy is the lowest when the vertical distance between Si and C increases to 6.5 $d_{(1\,1\,1)}$.

On this basis, the addition of C atoms to the supercells with two Si atoms is further studied. In each supercell, the Si atom far from the z-axis origin is defined as Si1 atom, and the other Si atom is defined as Si2 atom. As an example, a diagram based on supercell 2Si-6 is shown in Fig. 10(a). The C atoms are in the octahedral gap between the $(1\,1\,1)_\gamma$ crystal planes of the supercell, and the C site is defined as Position 1 and 2, respectively, when the C and two Si atoms are in the same and different $\left(\bar{1}\,10\right)_\gamma$ crystal planes. By varying the C position and the distance between C-Si1 and Si1-Si2, we built 100 different Fe-Si-C supercells. All structures were optimized based on an initial FCC structure of Fe after which the ELF was extracted. As can be seen from Fig. 10, there is a strong correlation between ELF and the structural transition from FCC-to-BCC based on the 100 structures. In general, the C doping can increase the ELF at the critical point of the Fe-Si bond. As a result, it promotes the phase transition in supercells to BCC structure when the ELF value is above 0.65, which is larger than ELF ($\sim$0.632) in Fe-Si bond in the corresponding FCC counterparts. Besides, C doping in the supercell in the same $\left(\bar{1}\,10\right)_\gamma$ plane of Si (i.e., position 1) will make the supercell more prone to crystal structure transformation. These results provide clear evidence for the correlation between electronic and crystal structure in steel.

5. Conclusions

In this work, by combining TEM analysis and DFT calculations, the physical mechanism of microstructure formation in the multiphase Fe-0.54C-2.53Si-1.82Mn-1.08Cr-0.45Ni-0.32Mo steel is studied. The main results were summarized as follows:

1. Si addition increases the ELF in γ-Fe, which improves the thermal stability of the γ-Fe and increases its SFE. Besides, Si addition significantly decreases the energy barrier for twin nucleation and martensite transformation and leads to large lattice distortion and Jahn-Keller splitting that resulted in a novel FCC-to-BCC phase transformation.
2. The hardness of the bainite steel is significantly improved due to the formation of multiple phases including BCC, FCC, ε-martensite, and nanotwinned structures by adding Si in it. The higher H/E and H3/E2 ratio of laser melting layer indicates its excellent resistance against elastic strain to failure and plastic deformation. The laser melting layer also shows good wear resistance.
3. A strong correlation between macroscopic properties of a material with its electronic structures is revealed, which suggests the possibility of engineering microstructures of materials by tailoring their electronic structures.

CRediT authorship contribution statement

Xiaolei Xing: Writing – original draft. **Yawen Li:** Writing – original draft, Investigation. **Shuo Meng:** . **Zhijun Shi:** . **Yefei Zhou:** Writing – original draft. **Qingxiang Yang:** Data curation. **Jianwei Xiao:** Writing – review & editing, Conceptualization, Methodology. **Yuntian Zhu:** . **Chuang Deng:** Project administration, Conceptualization, Writing – review & editing.

Data availability

Data will be made available on reasonable request.

Declaration of Competing Interest

The authors declare that they have no known competing financial interests or personal relationships that could have appeared to influence the work reported in this paper.

Acknowledgments

This work was supported by the National Natural Science Foundation of China (Grant No. 51905466), Natural Science Foundation of Hebei Province China (Grant Nos. E2020203184 and E2021203191), Youth Top Talent Project of Hebei Province Higher Education (Grant No. BJ2019058), and NSERC Discovery Grant (RGPIN-2019-05834), Canada. The authors also acknowledge the use of computing resources provided by WestGrid and Compute/Calcul Canada. The authors acknowledge Zhi Duan and Li Lou for performing the laser melting experiments and TEM analysis.

Appendix A. Supplementary data

Supplementary data to this article can be found online at https://doi.org/10.1016/j.matdes.2022.111011.

References

[1] L.G. Sun, G. Wu, Q. Wang, J. Lu, Nanostructural metallic materials: Structures and mechanical properties, Mater. Today 38 (2020) 114–135.
[2] M. Xu, Y.Q. Cheng, H.W. Sheng, E. Ma, Nature of Atomic Bonding and Atomic Structure in the Phase-Change Ge2Sb2Te5 Glass, Phys. Rev. Lett. 103 (19) (2009) 195502.
[3] E. Tea, J.Q. Huang, G.C. Li, C.L. Hin, Atomic bonding and electrical potential at metal/oxide interfaces, a first principle study, J. Chem. Phys. 146 (12) (2017).
[4] J. Mizuguchi, Correlation between Crystal and Electronic Structures in Diketopyrrolopyrrole Pigments as Viewed from Exciton Coupling Effects, J. Phys. Chem. A 104 (9) (2000) 1817–1821.
[5] J. Yu, Q. Xiang, M. Zhou, Preparation, characterization and visible-light-driven photocatalytic activity of Fe-doped titania nanorods and first-principles study for electronic structures, Appl. Catal. B-Environ. 90 (3) (2009) 595–602.
[6] J.F. Berry, F.A. Cotton, T. Lu, C.A. Murillo, B.K. Roberts, X. Wang, Molecular and Electronic Structures by Design: Tuning Symmetrical and Unsymmetrical Linear Trichromium Chains, J. Am. Chem. Soc. 126 (22) (2004) 7082–7096.
[7] V.V. Reshetniak, B.N. Mavrin, V.V. Medvedev, I.A. Perezhogin, B.A. Kulnitskiy, Optical properties of B12P2 crystals: Ab initio calculation and EELS, J. Phys. Chem. Solids. 116 (2018) 331–337.
[8] M. Heiss, S. Conesa-Boj, J. Ren, H.-H. Tseng, A. Gali, A. Rudolph, E. Uccelli, F. Peiró, J.R. Morante, D. Schuh, E. Reiger, E. Kaxiras, J. Arbiol, A., Fontcuberta i Morral, Direct correlation of crystal structure and optical properties in wurtzite/zinc-blende GaAs nanowire heterostructures, Phys. Rev. B 83 (4) (2011) 045303.
[9] Y. Sun, L. Zhao, Y. Zheng, M. Miao, The electron localizations and the corresponding chemical interactions that govern the structures of elemental metals, arXiv preprint arXiv:2109.09305 2109(09305) (2021).
[10] R. Chen, G. Qin, H. Zheng, L. Wang, Y. Su, Y. Chiu, H. Ding, J. Guo, H. Fu, Composition design of high entropy alloys using the valence electron concentration to balance strength and ductility, Acta Mater. 144 (2018) 129–137.
[11] J. Feng, B. Xiao, C.L. Wan, Z.X. Qu, Z.C. Huang, J.C. Chen, R. Zhou, W. Pan, Electronic structure, mechanical properties and thermal conductivity of Ln2Zr2O7 (Ln=La, Pr, Nd, Sm, Eu and Gd) pyrochlore, Acta Mater. 59 (4) (2011) 1742–1760.
[12] N. Li, K. Blankson, Y.F. Yang, P. Zhang, X.J. Zhao, Unraveling the electronic structure, mechanical, and dielectric properties of ZnPurBr-MOF: Ab initio calculations, Apl Mater. 8 (11) (2020).
[13] A.D. Liu, X.H. Zhang, Y.-J. Qiao, Impact of microscopic bonding on the thermal stability and mechanical property of CaB6: A first-principles investigation, Ceram. Int. 40(10, Part A) (2014) 15997–16002.

[14] K.B. Panda, K.S.R. Chandran, First principles determination of elastic constants and chemical bonding of titanium boride (TiB) on the basis of density functional theory, Acta Mater. 54 (6) (2006) 1641–1657.
[15] S. Ogata, J. Li, S. Yip, Ideal pure shear strength of aluminum and copper, Science 298 (5594) (2002) 807–811.
[16] X.H. An, S.D. Wu, Z.G. Wang, Z.F. Zhang, Significance of stacking fault energy in bulk nanostructured materials: Insights from Cu and its binary alloys as model systems, Prog. Mater. Sci. 101 (2019) 1–45.
[17] H. Chang, T.W. Zhang, S.G. Ma, D. Zhao, R.L. Xiong, T. Wang, Z.Q. Li, Z.H. Wang, Novel Si-added CrCoNi medium entropy alloys achieving the breakthrough of strength-ductility trade-off, Mater. Design. 197 (2021) 109202.
[18] S. Curtze, V.T. Kuokkala, Dependence of tensile deformation behavior of TWIP steels on stacking fault energy, temperature and strain rate, Acta Mater. 58 (15) (2010) 5129–5141.
[19] J.T. Lloyd, D.M. Field, K.R. Limmer, A four parameter hardening model for TWIP and TRIP steels, Mater. Design. 194 (2020) 108878.
[20] M. Jahnatek, J. Hafner, M. Krajci, Shear deformation, ideal strength, and stacking fault formation of fcc metals: A density-functional study of Al and Cu, Phys. Rev. B 79 (22) (2009).
[21] X. Tao, X. Liu, A. Matthews, A. Leyland, The influence of stacking fault energy on plasticity mechanisms in triode-plasma nitrided austenitic stainless steels: Implications for the structure and stability of nitrogen-expanded austenite, Acta Mater. 164 (2019) 60–75.
[22] D.E. Gomez, M. Califano, P. Mulvaney, Optical properties of single semiconductor nanocrystals, Phys. Chem. Chem. Phys. 8 (43) (2006) 4989–5011.
[23] Z.B. Zhuang, Q. Peng, Y.D. Li, Controlled synthesis of semiconductor nanostructures in the liquid phase, Chem. Soc. Rev. 40 (11) (2011) 5492–5513.
[24] D. Raabe, B.H. Sun, A.K. Da Silva, B. Gault, H.W. Yen, K. Sedighiani, P.T. Sukumar, I.R. Souza, S. Katnagallu, E. Jagle, P. Kurnsteiner, N. Kusampudi, L. Stephenson, M. Herbig, C.H. Liebscher, H. Springer, S. Zaefferer, V. Shah, S.L. Wong, C. Baron, M. Diehl, F. Roters, D. Ponge, Current Challenges and Opportunities in Microstructure-Related Properties of Advanced High-Strength Steels, Metall. Mater. Trans. A 51 (11) (2020) 5517–5586.
[25] M. Zorgani, C. Garcia-Mateo, M. Jahazi, Microstructural evolution during tempering of an ausformed carbide-free low temperature bainitic steel, Mater. Design. 210 (2021) 110082.
[26] S.H. Jiang, H. Wang, Y. Wu, X.J. Liu, H.H. Chen, M.J. Yao, B. Gault, D. Ponge, D. Raabe, A. Hirata, M.W. Chen, Y.D. Wang, Z.P. Lu, Ultrastrong steel via minimal lattice misfit and high-density nanoprecipitation, Nature 544 (7651) (2017) 460–464.
[27] R. Zhu, S. Li, I. Karaman, R. Arroyave, T. Niendorf, H.J. Maier, Multi-phase microstructure design of a low-alloy TRIP-assisted steel through a combined computational and experimental methodology, Acta Mater. 60 (6–7) (2012) 3022–3033.
[28] S. Ebner, C. Suppan, A. Stark, R. Schnitzer, C. Hofer, Austenite decomposition and carbon partitioning during quenching and partitioning heat treatments studied via in-situ X-ray diffraction, Mater. Design. 178 (2019) 107862.
[29] A. Królicka, A.M. Żak, F.G. Caballero, Enhancing technological prospect of nanostructured bainitic steels by the control of thermal stability of austenite, Mater. Design. 211 (2021) 110143.
[30] T. Voisin, J.-B. Forien, A. Perron, S. Aubry, N. Bertin, A. Samanta, A. Baker, Y.M. Wang, New insights on cellular structures strengthening mechanisms and thermal stability of an austenitic stainless steel fabricated by laser powder-bed-fusion, Acta Mater. 203 (2021) 116476.
[31] R. Li, Y. Jin, Z. Li, Y. Zhu, M. Wu, Effect of the remelting scanning speed on the amorphous forming ability of Ni-based alloy using laser cladding plus a laser remelting process, Surf. Coat. Tech. 259 (2014) 725–731.
[32] F.G. Caballero, H.K.D.H. Bhadeshia, Very strong bainite, Curr. Opin. Solid. St. M. 8 (3–4) (2004) 251–257.
[33] R. Ranjan, S.B. Singh, Isothermal bainite transformation in low-alloy steels: Mechanism of transformation, Acta Mater. 202 (2021) 302–316.
[34] C.W. Shao, P. Zhang, Y.K. Zhu, Z.J. Zhang, Y.Z. Tian, Z.F. Zhang, Simultaneous improvement of strength and plasticity: Additional work-hardening from gradient microstructure, Acta Mater. 145 (2018) 413–428.
[35] L. Ren, W. Xiao, D. Kent, M. Wan, C. Ma, L. Zhou, Simultaneously enhanced strength and ductility in a metastable β-Ti alloy by stress-induced hierarchical twin structure, Scripta Mater. 184 (2020) 6–11.
[36] X. Xing, Y. Zhou, X. Lu, X. Qi, L. Zhang, Q. Yang, Formation abilities of nano-twin and ε-martensite in laser surface modification of a mid-carbon steel, Appl. Surf. Sci. 479 (2019) 634–638.
[37] H.K.D.H. Bhadeshia, Cementite, Int. Mater. Rev. 65 (1) (2020) 1–27.
[38] M.D. Segall, P.J.D. Lindan, M.J. Probert, C.J. Pickard, P.J. Hasnip, S.J. Clark, M.C. Payne, First-principles simulation: ideas, illustrations and the CASTEP code, J. Phys.: Condens Matter. 14 (11) (2002) 2717.
[39] B. Hammer, L.B. Hansen, J.K. Nørskov, Improved adsorption energetics within density-functional theory using revised Perdew-Burke-Ernzerhof functionals, Physical Review B 59 (11) (1999) 7413–7421.
[40] G. Kresse, J. Hafner, Ab initio molecular dynamics for liquid metals, Phys. Rev. B 47 (1) (1993) 558–561.
[41] G. Kresse, J. Furthmüller, Efficiency of ab-initio total energy calculations for metals and semiconductors using a plane-wave basis set, Comp Mater Sci 6 (1) (1996) 15–50.
[42] M. Azuma, N. Fujita, M. Takahashi, T. Senuma, D. Quidort, T. Lung, Modelling upper and lower bainite trasformation in steels, Isij Int. 45 (2) (2005) 221–228.
[43] S. Zaefferer, J. Ohlert, W. Bleck, A study of microstructure, transformation mechanisms and correlation between microstructure and mechanical properties of a low alloyed TRIP steel, Acta Mater. 52 (9) (2004) 2765–2778.
[44] C. Garcia-Mateo, J.A. Jimenez, H.W. Yen, M.K. Miller, L. Morales-Rivas, M. Kuntz, S.P. Ringer, J.R. Yang, F.G. Caballero, Low temperature bainitic ferrite: Evidence of carbon super-saturation and tetragonality, Acta Mater. 91 (2015) 162–173.
[45] J. Lin, J.J. Moore, B. Mishra, M. Pinkas, W.D. Sproul, The structure and mechanical and tribological properties of TiBCN nanocomposite coatings, Acta Mater. 58 (5) (2010) 1554–1564.
[46] J. Xiao, N. Wu, O. Ojo, C. Deng, Electron localization governed plasticity in nanotwinned metals beyond the Hall-Petch type limit, Mat. Sci. Eng. A-Struct. 797 (2020) 140251.
[47] Y.H. Zhang, Y. Zhuang, A. Hu, J.J. Kai, C.T. Liu, The origin of negative stacking fault energies and nano-twin formation in face-centered cubic high entropy alloys, Scripta Mater. 130 (2017) 96–99.
[48] A.D. Becke, K.J.T.J.o.C.P. Edgecombe, A simple measure of electron localization in atomic and molecular systems, J. Chem. Phys. 92(9) (1990) 5397–5403.
[49] A. Savin, R. Nesper, S. Wengert, T.F. Fässler, ELF: The Electron Localization Function, Angew. Chem. Int. Edit. 36 (17) (1997) 1808–1832.
[50] R.F. Nalewajski, 4 - Probing the Molecular Electron Distributions, Inf. Theory Mol. Syst. (2006) 91–117.
[51] M.D. Sturge, The Jahn-Teller Effect in Solids, Solid. State. Phys. 20 (1968) 91–211.
[52] Q.M. Hu, R. Yang, Unconventional non-uniform local lattice distortion in dilute Ti-Mo solid solution, Acta Mater. 197 (2020) 91–96.